New Insights into the Structural Properties of Calcium Carbonate Hemihydrate by NMR Crystallography

Romain Chèvre,[1] Colan E. Hughes,[2] Samuel F. Cousin,[1] Marie Juramy,[1] Fabio Ziarelli,[3] Stéphane Viel,[1,4] Kenneth D. M. Harris,*[,2] Giulia Mollica,*[,1] Pierre Thureau*[,1]

1 Aix Marseille Univ, CNRS, ICR, Marseille, 13013, France

2 School of Chemistry, Cardiff University, Park Place, Cardiff, Wales, CF10 3AT, United Kingdom

3 Aix Marseille Univ, CNRS, Centrale Méditerranée, FSCM, Marseille, 13013, France

4 Institut Universitaire de France, Paris, 75005, France

Corresponding Authors

harriskdm@cardiff.ac.uk, giulia.mollica@univ-amu.fr, pierre.thureau@univ-amu.fr

Abstract

While calcium carbonate is well known to exist in a range of different crystalline forms, including anhydrous polymorphs and hydrated phases, a new crystalline form – calcium carbonate hemihydrate (CCHH) – was reported in 2019, and has recently been observed in a biogenic material. The crystal structure of CCHH reported from diffraction studies is monoclinic, although a subsequent computational investigation has suggested that an orthorhombic description of the structure may be more appropriate. Herein, we report experimental solid-state NMR characterization of CCHH, focused on solid-state ^{1}H NMR and ^{13}C NMR measurements, including analysis of ^{1}H-^{13}C heteronuclear correlation spectroscopy (HETCOR) and ^{13}C chemical shift anisotropy (CSA) data, which reveals further insights into the structural and symmetry properties of this material. We demonstrate by means of DFT-GIPAW calculations that the monoclinic and orthorhombic descriptions of the crystal structure of CCHH are readily distinguishable on the basis of solid-state ^{1}H NMR and ^{13}C NMR data. Our experimental solid-state NMR measurements are shown to support the orthorhombic description of the crystal structure rather than the monoclinic description.

1. Introduction

Calcium carbonate is an abundant material on Earth, and is the principal component in several geological materials (e.g., limestone and marble) and biological materials (e.g., shells and skeletons of marine organisms).[1-5] Calcium carbonate has been studied widely as a prototypical system in polymorphism research and in fundamental studies of crystallization processes.[6-8] In this regard, much of the interest in understanding the crystallization behaviour of calcium carbonate has been motivated by the importance of this material in biomineralization processes.[9-13]

Three crystalline polymorphs of calcium carbonate are known, specifically calcite,[14-17] aragonite[18-20] and vaterite.[21-26] The most stable polymorph is calcite, and the least stable is vaterite.[10,27,28] Crystalline hydrate phases of calcium carbonate ($CaCO_3.xH_2O$) are also known,[29] including ikaite (x = 6),[30-32] monohydrocalcite (x = 1; MHC),[33,34] and the recently reported calcium carbonate hemihydrate (x = 0.5; CCHH).[35] Depending on atmospheric conditions (i.e., temperature and humidity), the hydrate phases may undergo dehydration to form one of the anhydrous phases of calcium carbonate.[36-38] An amorphous phase of calcium carbonate is also known,[39-46] and is reported to be a hydrated phase.[40,47] Amorphous calcium carbonate is often observed as a transient phase on crystallization pathways, serving as a precursor to the formation of the crystalline phases discussed above.[41,48,49,50,51]

In the present paper, we focus on calcium carbonate hemihydrate (CCHH), which was first reported in 2019 by Zou *et al*.,[35] and has recently been observed as a component (together with MHC and amorphous precursors) in a biogenic system, specifically on freshly deposited coral skeleton and nacre surfaces.[52] The crystal structure reported[35] for CCHH (Figure 1a) was determined from analysis of electron diffraction data in conjunction with powder XRD studies, and is monoclinic ($P2_1/c$) with the following unit cell parameters (at 293 K): a = 9.331 Å, b = 10.436 Å, c = 6.162 Å, β = 90.52°; V = 600.0 Å^3. In this monoclinic structure, the asymmetric unit comprises two calcium cations, two carbonate anions and one water molecule. The locations of the H atoms of the water molecule were not specified in the reported structure, and therefore the H-bonding arrangement in the crystal structure was not assigned. Furthermore, the two independent carbonate anions in the reported structure both deviate significantly from normal geometric features for carbonate anions. In the

discussion below, we refer to the two independent carbon environments in the monoclinic structure as C1 and C2 (see Figure 1a); in the reported crystal structure,[35] the fractional coordinates of C1 and C2 are (0.604, 0.846, 0.254) and (0.112, 0.669, 0.224), respectively.

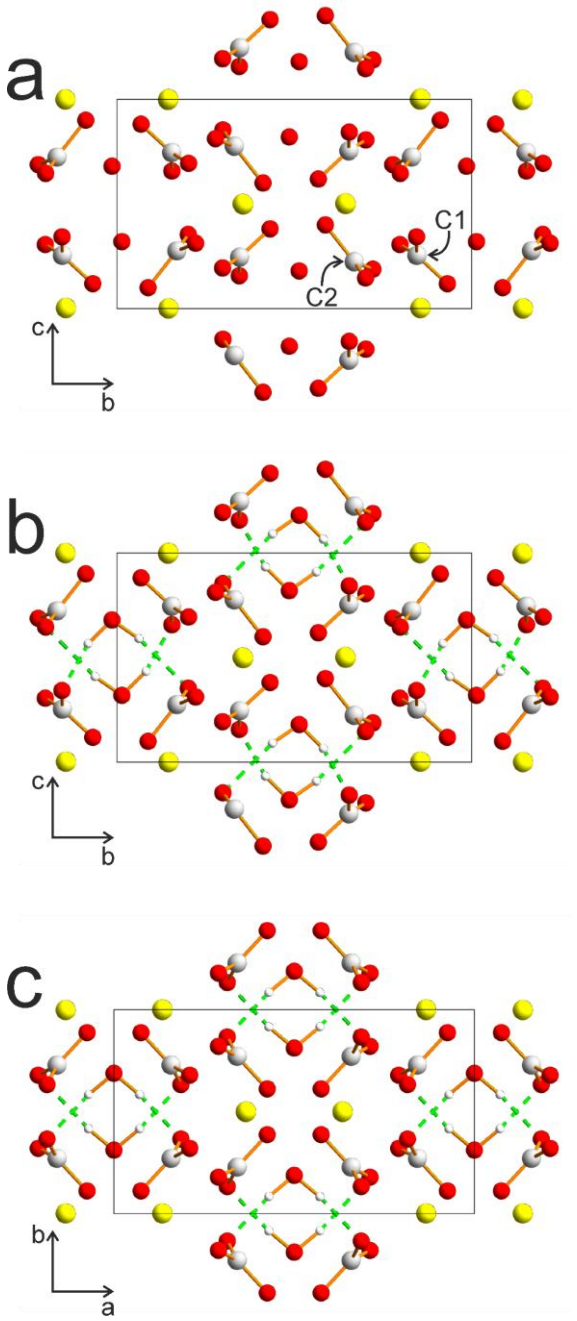

Figure 1. (a) The monoclinic structure of CCHH (space group $P2_1/c$) reported by Zou et *al*.[35] (the positions of H atoms were not reported); the two independent carbon environments (C1 and C2) in this structure are indicated. (b) The monoclinic structure of CCHH used in the present work to calculate solid-state NMR properties; the positions of the non-H atoms are identical to those in the reported structure[35] shown in (a), with the H atoms of the water molecule added in optimized positions corresponding to a favourable H-bonding arrangement (see Section 2.2). (c) The orthorhombic structure of CCHH (space group Pbcn); in this structure, the water molecules are located on two-fold rotation axes parallel to the *b*-axis. Carbon, grey; hydrogen, white; oxygen, red; calcium, yellow. H-bonding is indicated by green dashed lines.

A subsequent computational study by Aufort and Demichelis investigated structural properties of CCHH using periodic dispersion-corrected Density Functional Theory (DFT-D) methods.[53] This work led to an assignment of the positions of the H atoms of the water molecule and to improved geometries of the carbonate anions. Furthermore, periodic DFT-D calculations (using the PBE0-DC functional and dispersion correction) starting from the monoclinic structure with H atoms included led, following geometry optimization with relaxation of the unit cell, to a final geometry optimized structure (a = 9.322 Å, b = 10.477 Å, c = 6.061 Å; V = 592.0 Å^3) with orthorhombic crystal symmetry described by space group Pnca (an unconventional setting of space group Pbcn).[1] The orthorhombic structure is shown in Figure 1c based on the conventional Pbcn space group setting, which is used throughout the present paper. In contrast to the monoclinic structural description reported by Zou *et al*.,[35] the asymmetric unit in the orthorhombic structure contains one calcium cation, one carbonate anion and one-half water molecule (the O atom of the water molecule is located on a 2-fold rotation axis, with one H atom in the asymmetric unit).

In order to further explore the structural properties of CCHH with a view to assessing whether the monoclinic or orthorhombic description is more appropriate, we note that solid-state nuclear magnetic resonance (NMR) techniques are generally sensitive to details of the structural and symmetry properties of crystalline materials,[54-69] and may therefore be able to provide additional insights to those obtained from the previous investigations of CCHH.[35,53] In the present work, we report the first experimental solid-state NMR studies of CCHH, focusing on solid-state ^{1}H and ^{13}C NMR measurements, and including analysis of the ^{1}H-^{13}C HETCOR spectrum and ^{13}C chemical shift anisotropy (CSA) data. Our analysis of the experimental solid-state NMR data also includes comparisons with solid-state NMR data calculated using DFT-GIPAW methodology[70-74] for the monoclinic and orthorhombic descriptions of the structure of CCHH. For comparative purposes, we have also recorded solid-state ^{13}C NMR data for several other phases (both anhydrous and hydrate phases) of calcium carbonate.

[1] The work of Aufort and Demichelis[53] also investigated the effects of incorporating Mg^{2+} ions within the structure of CCHH on the structural and energetic properties. However, we note that the molar percentages of Mg^{2+} (relative to total Ca^{2+} and Mg^{2+}) considered in their computational studies (ranging from 3.125% to 100%) were higher than the molar percentage of Mg^{2+} (1.9%) determined for the experimental sample of CCHH reported previously[35] (1.9% is calculated based on the data in Table S1 of ref. 35).

2. Results and Discussion

2.1 Sample Preparation and Characterization

All samples of CCHH were prepared using the procedure described in Section 4.1, which is based on the methods reported previously.[35] Powder XRD data (Figure 2) recorded for samples of CCHH prepared using this procedure are in good agreement with the powder XRD data reported previously[35] for CCHH (see Figure 1 in ref. 35), confirming that the samples studied here represent the same crystalline phase as the material assigned previously as CCHH.

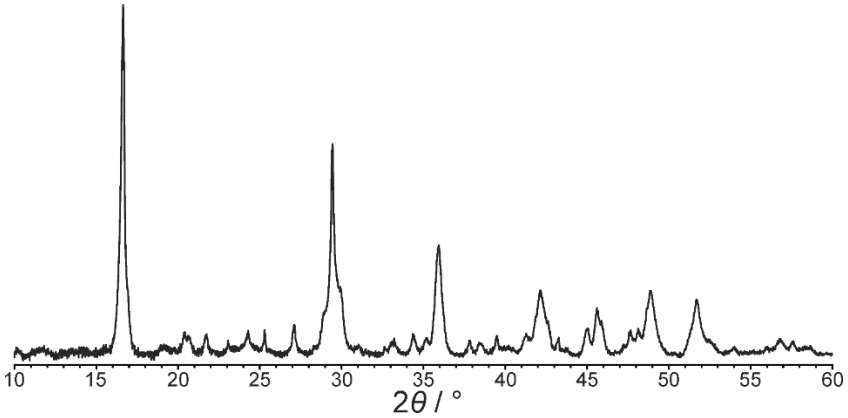

Figure 2. Powder XRD data recorded (λ = 1.5406 Å) for a freshly prepared sample of CCHH, which is representative of the powder XRD data for the samples of CCHH studied in the present work.

2.2 Generating the Monoclinic and Orthorhombic Structures of CCHH for DFT-GIPAW Calculations of Solid-state NMR Data

As the monoclinic structure of CCHH reported by Zou *et al*.[35] does not contain H atoms, it is necessary to generate a version of this structure containing the H atoms of the water molecules in order to be able to carry out DFT-GIPAW calculations of solid-state NMR data. For this purpose, several positions of the H atoms were considered such that O–H···O interactions between the water molecules and carbonate anions are formed with geometrically reasonable H-bond distances and H-bond angles, but with the positions of all non-H atoms corresponding to those in the reported crystal structure.[35] Each of these structural models was subjected to DFT-D geometry optimization in which only the positions of the H atoms were allowed to vary (thus, the positions of the non-H atoms were fixed, the unit cell parameters were fixed, and the space group symmetry was preserved). For all the

starting structures (with different H atom positions) considered, the DFT-D geometry optimization calculations converged on the same optimized structure (i.e. with the same H atom positions). This optimized structure (shown in Figure 1b) was used in all subsequent DFT-GIPAW calculations of NMR properties for the monoclinic structure.

In the present work, the orthorhombic structure of CCHH was generated by DFT-D geometry optimization, starting from the monoclinic structure (including H atoms) described above and including relaxation of the unit cell within the geometry optimization procedure. Although the resulting geometry optimized structure was still described by the original monoclinic space group, the unit cell β angle converged from the value ($\beta = 90.52°$) in the starting monoclinic structure to a value ($\beta = 89.99°$) very close to 90°, corresponding to orthorhombic metric symmetry. Furthermore, it was clear that the atomic positions in the geometry optimized structure actually corresponded to orthorhombic crystal symmetry (space group Pbcn). This structure was then transformed into a strict orthorhombic description (with orthorhombic metric symmetry and space group Pbcn) and then subjected to further DFT-D geometry optimization, including relaxation of the unit cell. The final structure resulting from this DFT-D geometry optimization (shown in Figure 1c) was taken as the orthorhombic structure for all DFT-GIPAW calculations of solid-state NMR properties. We note that this structure corresponds to the orthorhombic structure proposed by Aufort and Demichelis,[53] and has the same H-bonding arrangement. More detailed comparison of the monoclinic and orthorhombic structural descriptions of CCHH is given in Section S4.

For comparative purposes (discussed in Section S5), we also generated a structure (referred to as the "relaxed monoclinic structure") by DFT-D geometry optimization, starting from the monoclinic structure described above (i.e., the structure reported by Zou *et al*.[35] but including the H atoms of the water molecule). In the DFT-D geometry optimization, the unit cell and space group ($P2_1/c$) were fixed and only the atomic positions were relaxed. As discussed in Section S5, the "relaxed monoclinic structure" resulting from this DFT-D geometry optimization is essentially identical to the orthorhombic structure (although still based on a unit cell with monoclinic metric symmetry and with crystal symmetry described by a monoclinic space group).

2.3 Solid-State NMR Studies

High-resolution solid-state ^{13}C NMR spectra were recorded in the present work for various crystalline phases of calcium carbonate (specifically, CCHH, ikaite, MHC, calcite and aragonite), as shown in Figure 3. For CCHH, ikaite and MHC, the solid-state ^{13}C NMR spectrum was recorded using the $^{1}H \rightarrow ^{13}C$ cross-polarization (CP) NMR technique. For calcite and aragonite, the solid-state ^{13}C NMR spectrum was recorded using the direct-excitation ^{13}C NMR technique (as these phases do not contain hydrogen, they would not give a signal in $^{1}H \rightarrow ^{13}C$ CP NMR measurements). The isotropic ^{13}C NMR chemical shifts determined from the experimental solid-state ^{13}C NMR spectra for ikaite, MHC, calcite and aragonite (Figure 3b-e) are in good agreement with experimental values reported previously (Table S1). Furthermore, our DFT-GIPAW calculated values of the isotropic ^{13}C NMR chemical shifts for these phases are in agreement with the experimental data, as also shown in Table S1.

In our work, each solid-state NMR measurement was carried out on a freshly prepared sample of CCHH. As the measurement of high-resolution solid-state NMR data requires the application of magic-angle sample spinning (MAS), it is important to assess whether the pressure effects that arise from the application of MAS[75-77] cause any changes to the sample (for example, by inducing solid-state phase transitions or dehydration of hydrate phases). To assess this issue, powder XRD data (Figure S4) were recorded for a sample of CCHH before and after a solid-state NMR measurement in which MAS was applied at 5 kHz for 15 mins at 270 K. As the powder XRD patterns recorded before and after the solid-state NMR measurement both correspond to the powder XRD pattern characteristic of CCHH, we conclude that the application of MAS under these conditions does not cause any significant changes to the sample. Furthermore, all solid-state NMR experiments were conducted with temperature control to avoid dehydration of the sample of CCHH or other structural transformations.

The high-resolution solid-state ^{13}C NMR spectrum recorded for CCHH at 293 K (Figure 3a) contains a single isotropic peak at 166.1 ppm, which is clearly distinct from the isotropic ^{13}C chemical shifts characteristic of the other solid phases of calcium carbonate studied herein (Figure 3). At low temperature (100 K), the solid-state ^{13}C NMR spectrum of CCHH also contains a single peak (at

165.9 ppm), and the similarity to the spectrum recorded at 293 K suggests that CCHH does not undergo any phase transition between these temperatures.

The fact that a single isotropic peak is observed in the solid-state ^{13}C NMR spectrum of CCHH is fully consistent with the orthorhombic structural description, for which there is only one ^{13}C environment in the asymmetric unit. In contrast, the monoclinic structural description has two crystallographically independent ^{13}C environments and would therefore be expected to exhibit two distinct isotropic peaks in the solid-state ^{13}C NMR spectrum. To investigate this issue more quantitatively, the isotropic ^{13}C NMR chemical shifts for the monoclinic and orthorhombic structures were calculated using DFT-GIPAW methodology to be 169.1 ppm (C1) and 179.2 ppm (C2) for the two ^{13}C environments in the monoclinic structure (C1 and C2 in Figure 1a), and 165.3 ppm for the single ^{13}C environment in the orthorhombic structure. As shown in Figure 4, better agreement is clearly observed between the experimental solid-state ^{13}C NMR spectrum and the DFT-GIPAW calculated solid-state ^{13}C NMR data for the orthorhombic structure than for the monoclinic structure.

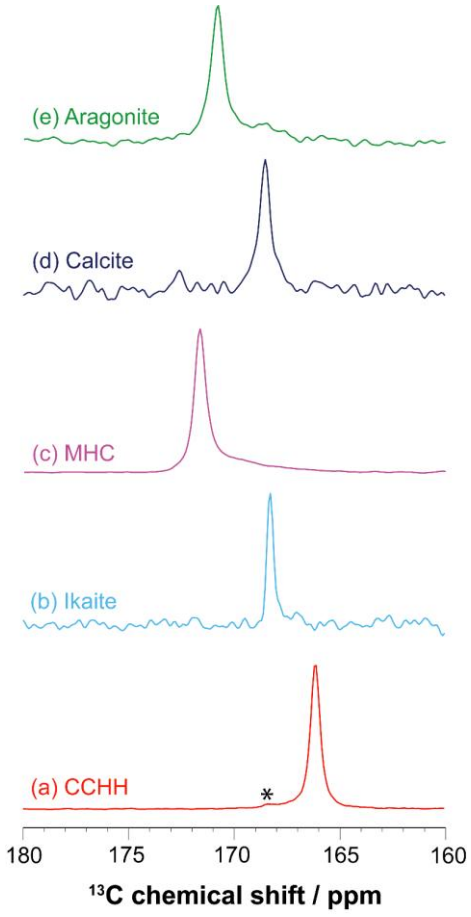

Figure 3. Experimental high-resolution solid-state ^{13}C NMR spectra recorded (^{13}C Larmor frequency, 100.65 MHz; MAS frequency, 8 kHz) for: (a) CCHH, (b) ikaite, (c) MHC, (d) calcite, and (e)

aragonite. The spectra in (a), (b) and (c) were recorded using $^{1}H \rightarrow ^{13}C$ CP NMR ($^{1}H \rightarrow ^{13}C$ CP contact time, 4 ms). The spectra in (d) and (e) were recorded using direct-excitation ^{13}C NMR. The spectrum for ikaite was recorded at 100 K; all other spectra were recorded at 293 K. In (a), the feature marked * suggests the presence of a small impurity in the sample, with ^{13}C chemical shift close to that of ikaite.

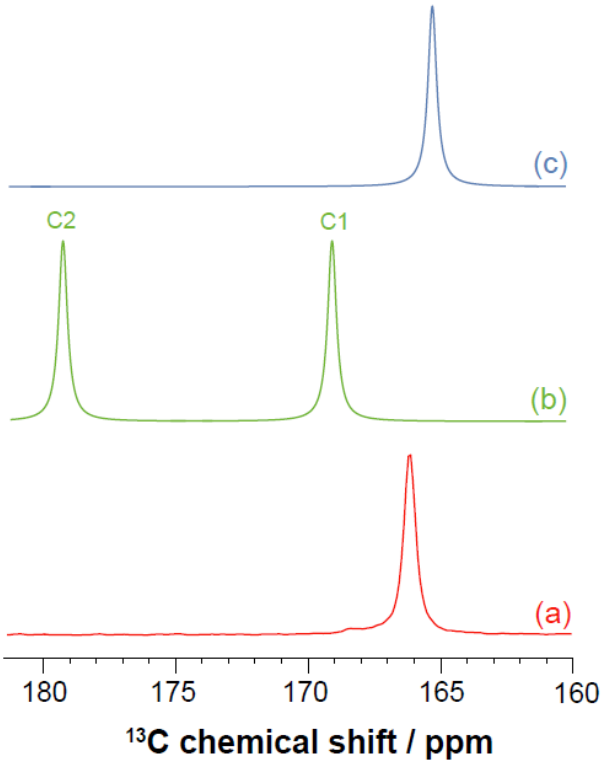

Figure 4. (a) Experimental high-resolution solid-state ^{13}C NMR spectrum recorded for CCHH at 293 K (^{13}C Larmor frequency, 100.65 MHz; MAS frequency, 8 kHz; $^{1}H \rightarrow ^{13}C$ CP contact time, 4 ms), (b) DFT-GIPAW calculated solid-state ^{13}C NMR spectrum for the monoclinic structure of CCHH, and (c) DFT-GIPAW calculated solid-state ^{13}C NMR spectrum for the orthorhombic structure of CCHH. The method for referencing the DFT-GIPAW calculated solid-state ^{13}C NMR spectra is discussed in Section 4.5.

The ^{1}H-^{13}C FSLG HETCOR NMR spectrum recorded for CCHH at 100 K is shown in Figure 5a. From this spectrum, it is clear that the sample of CCHH used for this measurement also contained minor amounts of MHC and ikaite. For each phase present in the sample, the solid-state ^{1}H NMR spectrum extracted from the ^{1}H-^{13}C HETCOR data is shown in Figure 5b. For CCHH, the solid-state ^{1}H NMR spectrum contains a single isotropic peak at 3.9 ppm, which is clearly distinct from the isotropic peaks assigned to the minor phases in the sample (5.4 ppm for MHC; 4.5 ppm for ikaite). The fact that the solid-state ^{1}H NMR spectrum of CCHH contains a single isotropic peak (Figure 5b; Table S1) is again consistent with the orthorhombic description of the crystal structure, which has only one ^{1}H environment in the asymmetric unit. Moreover, better agreement is clearly observed between the experimentally determined value of the isotropic ^{1}H chemical shift (3.9 ppm) for CCHH

and the DFT-GIPAW calculated value for the ^{1}H site in the orthorhombic structure (5.3 ppm) than the DFT-GIPAW calculated values (2.1 ppm and 7.0 ppm) for the two independent ^{1}H sites in the monoclinic structure.

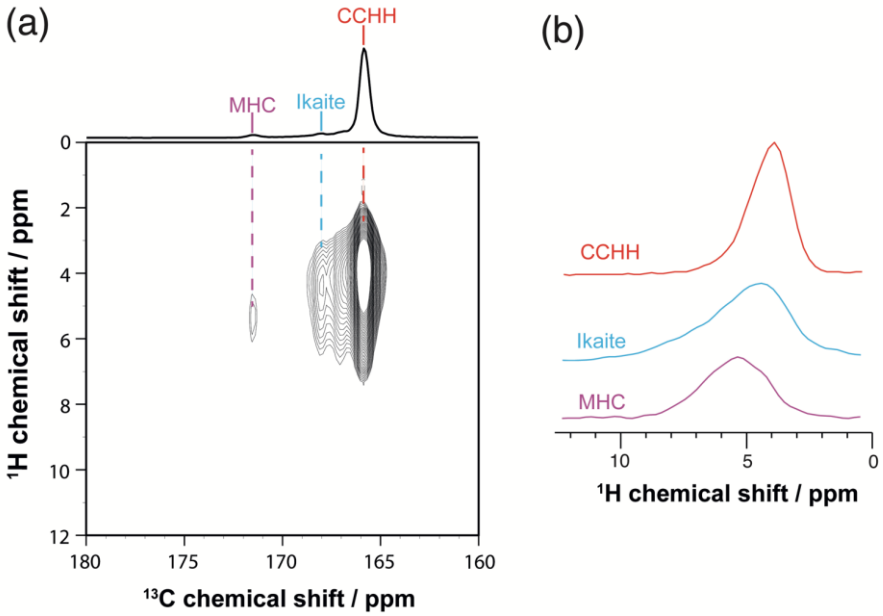

Figure 5. (a) ^{1}H-^{13}C FSLG HETCOR NMR spectrum recorded at 100 K and with an MAS frequency of 8 kHz for a sample of CCHH containing minor amounts of MHC and ikaite (^{1}H Larmor frequency, 400.21 MHz; ^{13}C Larmor frequency, 100.65 MHz; ^{1}H→^{13}C CP contact time, 4 ms). Intensity contour intervals are defined on a linear scale. The 1D solid-state ^{13}C NMR spectrum shown at the top is a ^{1}H→^{13}C CPMAS NMR spectrum recorded independently for the same sample of CCHH. (b) Solid-state ^{1}H NMR spectra for CCHH, MHC and ikaite extracted from the ^{1}H-^{13}C FSLG HETCOR spectrum in (a).

We now consider ^{13}C chemical shift anisotropy (CSA) data for CCHH recorded using the SUPER pulse sequence.[78] The experimental ^{13}C CSA powder pattern is shown in Figure 6a, together with simulated ^{13}C CSA powder patterns based on the DFT-GIPAW calculated ^{13}C CSA parameters (Table 1) for the monoclinic (Figure 6b) and orthorhombic (Figure 6c) structures. While the simulated ^{13}C CSA powder patterns for the monoclinic and orthorhombic structures are both in relatively good agreement with the experimental ^{13}C CSA powder pattern, overall better agreement is observed for the orthorhombic structure. Specifically, in the regions of highest (*ca.* 200 – 230 ppm) and lowest (*ca.* 110 – 140 ppm) ^{13}C chemical shift, the shape of the powder pattern for the monoclinic structure differs significantly from the experimental powder pattern, reflecting the existence of two distinct ^{13}C sites with appreciably different ^{13}C CSA parameters (Table 1) for the monoclinic structure. Furthermore, considering the value of ^{13}C chemical shift corresponding to maximum intensity (at *ca.* 180 ppm) in the ^{13}C CSA powder pattern, the monoclinic structure shows significantly greater

deviation from the experimental powder pattern than the orthorhombic structure. While the agreement between the experimental ^{13}C CSA powder pattern and the simulated ^{13}C CSA powder pattern for the orthorhombic structure is not perfect (e.g., the overall width of the experimental powder pattern is broader by a few ppm), the agreement is clearly better than that for the monoclinic structure.

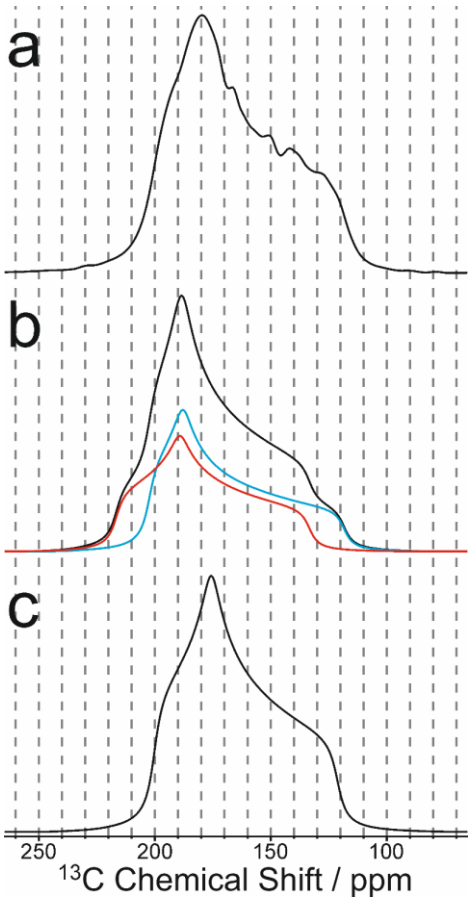

Figure 6. (a) Experimental ^{13}C CSA powder pattern recorded (^{13}C Larmor frequency, 100.65 MHz) for CCHH, and (b, c) simulated ^{13}C CSA powder patterns based on DFT-GIPAW calculated ^{13}C CSA parameters for (b) the monoclinic structure and (c) the orthorhombic structure. The simulated ^{13}C CSA powder patterns used a linewidth parameter (for an individual crystal orientation) of $W = 3$ ppm. In (b), the individual ^{13}C CSA powder patterns for ^{13}C sites C1 and C2 in the monoclinic structure are shown in cyan and red respectively.

Table 1. DFT-GIPAW calculated values of the isotropic ^{13}C NMR chemical shift (δ_{iso}), anisotropy (σ_{aniso}) and asymmetry (η) for each crystallographically independent ^{13}C site in the monoclinic and orthorhombic structures. The method for referencing the calculated isotropic ^{13}C chemical shifts is described in Section 4.5.

	Monoclinic		**Orthorhombic**
^{13}C site	C1	C2	C1
δ_{iso} / ppm	169.1	179.2	165.3
δ_{aniso} / ppm	–50.9	–46.3	–44.1
η	0.28	0.59	0.55

Analysis of the experimental ^{13}C CSA data was also carried out by fitting using models based on one ^{13}C site (Model 1) and two independent ^{13}C sites (Model 2). For Model 1, the fitting involved four variable parameters: three ^{13}C CSA parameters (δ_{iso}, δ_{aniso}, η) and a parameter (W) representing the linewidth for an individual crystal orientation. For Model 2, the fitting involved seven variable parameters: three ^{13}C CSA parameters for each of the two ^{13}C sites and the linewidth parameter W. As discussed in more detail in Supporting Information (Section S2), Models 1 and 2 both give a good fit to the experimental ^{13}C CSA powder pattern (Figures S2, S3), with a slightly better fit observed for Model 2. However, for Model 1, a unique set of best-fit parameters is obtained (Table S2; Figure S2), whereas for Model 2, essentially the same quality of fit to the experimental data is obtained for several alternative sets of parameters (Table S3; Figure S3), with particularly significant variations in the values of δ_{aniso} and η among these sets of parameters. The fact that a unique set of best-fit parameters is not obtained for Model 2 suggests that there is a problem with overfitting the data in this case (arising from the higher number of variable parameters for the model with two ^{13}C CSA sites). On this basis, we conclude that the experimental ^{13}C CSA powder pattern is most satisfactorily described by a single ^{13}C site, which is consistent with the orthorhombic structure of CCHH.

3. Concluding Remarks

We have reported an experimental solid-state ^{1}H and ^{13}C NMR characterization of CCHH, including a detailed comparison of various aspects of the experimental solid-state NMR data with the corresponding DFT-GIPAW calculated solid-state NMR data for the monoclinic and orthorhombic descriptions of the crystal structure of CCHH. Overall, our experimental solid-state NMR data are in better agreement with the orthorhombic description than the monoclinic description, thus supporting the assignment that the crystal structure of CCHH is orthorhombic.

Future studies involving a combination of solid-state ^{43}Ca NMR, powder XRD and crystal structure prediction are anticipated to lead to further insights into the structural properties of CCHH. From the computational viewpoint, future work implementing higher levels of theory for DFT-GIPAW calculations of solid-state NMR data for CCHH may also be informative, for example using methodology reported recently to implement the PBE0 functional in more accurate calculations of solid-state NMR data.[68] Finally, while the results from our solid-state NMR studies reported in this

paper support the orthorhombic structural description of CCHH, we note that (as discussed in Section S3) future plans include a detailed analysis of the experimental powder XRD pattern of CCHH with the aim of establishing a consistent interpretation of the structural properties of CCHH across all experimental techniques.

4. Methods

4.1 Sample Preparation

Powder samples of CCHH were prepared by the following procedure, which is slightly adapted from the procedure reported by Zou *et al*.[35] A solution containing carbonate ions was prepared by dissolving $Na_2CO_3 \cdot 10H_2O$ (2 mmol) in water (HPLC Plus grade; 48 mL), and a solution containing calcium ions was prepared by dissolving $CaCl \cdot 2H_2O$ (42.5 mmol) and $MgCl \cdot 6H_2O$ (7.5 mmol) in water (HPLC Plus grade; 50 mL). An amount (2 mL) of the calcium containing solution was then added to the whole amount (48 mL) of the carbonate containing solution, with the composition of the resulting solution (total volume *ca*. 50 mL) corresponding to: $CaCl_2 \cdot 2H_2O$ (1.7 mmol), $MgCl_2 \cdot 6H_2O$ (0.3 mmol) and $Na_2CO_3 \cdot 10H_2O$ (2 mmol). We note that the reason to include magnesium ions in the solution is to inhibit the formation of calcite. Upon mixing the two solutions, precipitation occurred instantly, and the solution was then stirred for 2000 s at ambient temperature. The precipitate was then filtered immediately under vacuum, rinsed with ethanol, and the powder sample was stored at 253 K. The molar percentage of Mg^{2+} (relative to total Ca^{2+} and Mg^{2+}) for the samples of CCHH prepared in this work was determined to be 1.3% from elemental analysis. This value is consistent with the magnesium content in CCHH samples prepared previously using this procedure,[35] which corresponded to a molar percentage of Mg^{2+} (relative to total Ca^{2+} and Mg^{2+}) of 1.9%.

4.2 Powder XRD

Powder XRD data were recorded on a Bruker D8 diffractometer operating in transmission mode (Ge monochromated Cu $K\alpha_1$ radiation, λ = 1.5406 Å; Våntec detector covering 3° in 2θ; step size 0.016°). A foil-type sample holder was used, with the powder sample held between two pieces of adhesive tape. The powder XRD pattern of CCHH shown in Figure 2 was recorded as 70 powder XRD datasets measured consecutively with the same acquisition parameters (2θ range, 10 – 70°; time

per dataset, 4.35 hr; total data collection time for 70 datasets, 304.5 hr). No change in the powder XRD pattern was observed between the first dataset and the last (70th) dataset. The 70 datasets were summed to give the powder XRD pattern shown in Figure 2.

For some samples, the powder XRD data were recorded at ambient temperature using a Rigaku RU-200BH instrument with a high-brightness copper anode (CuKα radiation; λ = 1.5418 Å; beam size, 0.5 × 0.5 mm^2), a double reflection focusing optic (OSMIC), and a Mar345 type 2D detector.

4.3 Solid-State NMR Spectroscopy

Each solid-state NMR experiment was carried out on a freshly prepared sample of CCHH.

Solid-state NMR data were primarily recorded on a Bruker AVANCE-III NMR spectrometer (at Aix Marseille University) with a Bruker 9.4 T wide-bore magnet (^{1}H and ^{13}C Larmor frequencies 400.21 MHz and 100.65 MHz, respectively) and either a Bruker 3.2 mm double-resonance ^{1}H/^{13}C CPMAS probe or a Bruker 3.2 mm low-temperature double-resonance DNP ^{1}H/{^{29}Si/^{13}C} CPMAS probe. The ^{13}C chemical shift was externally referenced using the signal for the carboxylate ^{13}C environment in the α polymorph of glycine, which was set to 176.5ppm.[79, 80]

^{1}H→^{13}C CPMAS NMR spectra were recorded at ambient temperature (293 K) with 8196 repetitions (MAS frequency, ν_R = 8 kHz; CP contact time, 4 ms; recycle delay, 2 s; the radio frequency (rf) for the ^{1}H 90° pulse was 100 kHz. ^{1}H decoupling was applied during acquisition, using SPINAL64[81] with rf nutation frequency of 100 kHz. The contact pulse on ^{1}H was ramped linearly from 50 kHz to 100 kHz and the ^{13}C CP spin-lock rf amplitude was 55 kHz.

Direct-excitation ^{13}C NMR spectra were recorded at ambient temperature with 640 repetitions (MAS frequency, ν_R = 8 kHz; recycle delay, 180 s; ^{13}C 30° pulse at 100 kHz).

Chemical shift anisotropy (CSA) ^{13}C NMR powder patterns were recorded at 253 K using the ^{13}C-SUPER pulse sequence.[78] In this measurement, the ^{13}C CSA powder pattern represents a slice at the isotropic ^{13}C chemical shift for CCHH, and therefore does not contain contributions from any other phases in the sample (e.g., impurities amounts of other phases of calcium carbonate). This 2D experiment was performed with MAS frequency ν_R = 5.5 kHz, using $\omega_{RF}(^1H)/2\pi$ = 100 kHz (the

amplitude of the ^{1}H rf field was ramped during the ^{1}H→^{13}C CP contact time to improve CP efficiency) and $\omega_{RF}(^{13}C)/2\pi$ = 47 kHz for cross-polarization. For the ^{13}C CSA recoupling 360° pulse, the rf nutation frequency was 12.12 × ν_R = 67 kHz, leading to a pulse length of 15 μs. Under these experimental conditions, the scaling factor in the indirect dimension of the 2D spectrum was 0.15.[78] Refocusing the CSA Hamiltonian occurs with ^{1}H decoupling switching from 65 to 25 kHz during ^{13}C irradiation. In addition to CSA refocusing, a four-pulse suppression of sidebands (TOSS) sequence was applied before detection (see Figure S2 in SI). The States-TPPI procedure was used to achieve a pure Lorentzian lineshape in both dimensions.[82] The ^{13}C NMR signal was acquired with ^{1}H decoupling at a nutation frequency of 60 kHz. The 1D ^{13}C CSA powder pattern of CCHH was extracted from the indirect dimension of the 2D SUPER spectrum by selecting the column corresponding to the isotropic ^{13}C chemical shift of CCHH in the direct dimension. The resulting spectrum was then shifted to match the isotropic ^{13}C chemical shift of CCHH, as described in ref. [78]. The principal values of the chemical shift tensors (δ_{xx}, δ_{yy}, δ_{zz}) are defined according to $|\delta_{zz} - \delta_{iso}| \geq |\delta_{xx} - \delta_{iso}| \geq |\delta_{yy} - \delta_{iso}|$, and δ_{aniso} is defined as $\delta_{aniso} = \delta_{zz} - \delta_{iso}$.

The ^{1}H-^{13}C FSLG HETCOR spectrum was recorded at 100 K with 16 repetitions. The FID comprised 256 complex points in t_1 and 2048 points in t_2 (MAS frequency, 8 kHz; recycle delay, 3 s). Homonuclear FSLG ^{1}H decoupling was applied with a 96 kHz ^{1}H field during t_1 and a ^{1}H→^{13}C CP contact time of 4 ms was used under Lee-Goldburg conditions. Pure absorption 2D NMR spectra were recorded using the States-TPPI procedure. During acquisition, ^{1}H decoupling was applied at a nutation frequency of 89 kHz. Calibration of ^{1}H chemical shifts was based on the ^{1}H NMR signal of the minor amount of monohydrocalcite present in the sample, which was set at 5.4 ppm.[47]

Additional solid-state ^{13}C NMR spectra were recorded on a Bruker AVANCE-III HD NMR spectrometer (at Cardiff University) with a Bruker 9.4 T wide-bore magnet (^{1}H and ^{13}C Larmor frequencies 400.20 MHz and 100.64 MHz, respectively) and a 4 mm MAS double-resonance ^{1}H/{^{14}N/^{31}P} probe. The experiments were carried out with an MAS frequency of 5 kHz, CP contact time of 1.5 ms, recycle delay of 4 s, and a ^{1}H 90° pulse at 71 kHz. ^{1}H decoupling was applied during acquisition, using SPINAL64 with a nutation frequency of 71 kHz. The temperature (270 K) was calibrated using methanol.[83-85]

4.4 DFT-D Studies to Generate the Monoclinic and Orthorhombic Structures of CCHH

Periodic DFT-D geometry optimization calculations were carried out using CASTEP[70] (Academic Release version 21). These calculations used ultrasoft pseudopotentials,[86] PBE functional,[87] semi-empirical dispersion correction using the TS correction scheme,[88] preserved space group symmetry, periodic boundary conditions, a basis set cut-off energy of 700 eV and a Monkhorst-Pack grid[89] of minimum sample spacing ($0.05 \times 2\pi$) $Å^{-1}$. The convergence criteria for geometry optimization were 0.01 eV $Å^{-1}$ for the maximum atomic force, 0.00001 eV per atom on the total energy, and 0.001 Å for atomic displacements. The DFT-D geometry optimization calculations were carried out with preservation of space group symmetry and either with fixed unit cell or with relaxation of the unit cell.

4.5 DFT-GIPAW Calculations of Solid-State NMR Data

Solid-state NMR data were calculated for the DFT-D geometry-optimized monoclinic and orthorhombic structures of CCHH (generated as described in Section 2.2) using the Gauge Including Projector Augmented Wave (GIPAW) approach[70-72,74] in the program CASTEP[70] (Academic Release version 21). These calculations used ultrasoft pseudopotentials,[86] the PBE exchange-correlation functional[46] with cut-off energy 800 eV, and the TS correction scheme[47] for dispersion correction.

For DFT-GIPAW calculations of solid-state ^{13}C NMR data, the isotropic ^{13}C NMR chemical shift (δ_{calc}) for each ^{13}C environment in the crystal structure was determined from the corresponding DFT-GIPAW calculated value of isotropic ^{13}C NMR shielding (σ_{calc}) using the equation:[54]

$$\delta_{calc} = \sigma_{ref} - \sigma_{calc} \quad (1)$$

The value of σ_{ref} = (170.2 ± 0.7) ppm was determined from linear regression between the DFT-GIPAW calculated values of isotropic ^{13}C NMR shielding (σ_{calc}) and the experimental isotropic ^{13}C NMR chemical shifts (δ_{exp}) for four solid phases of calcium carbonate, specifically aragonite (ICSD collection code 32100),[90] calcite (ICSD collection code: 166365),[91] ikaite (ICSD collection code: 16070)[31] and MHC (ICSD collection code: 160811),[34] as shown in Figure 7. The line in Figure 7 represents the linear regression between values of σ_{calc} and δ_{exp}, based on the equation:

$$\sigma_{calc} = \sigma_{ref} - \delta_{exp} \quad (2)$$

(i.e., with a gradient of –1 imposed for the best-fit line). The value of σ_{ref} determined from the linear regression was σ_{ref} = (170.2 ± 0.7) ppm.

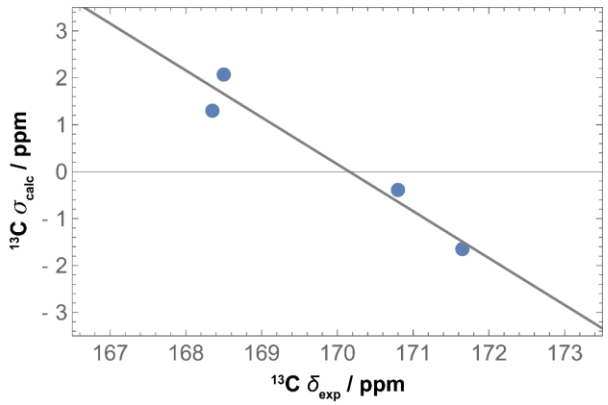

Figure 7. Correlation between DFT-GIPAW calculated values of isotropic ^{13}C NMR shielding (σ_{calc}) and experimentally measured values of isotropic ^{13}C NMR chemical shift (δ_{exp}) for different solid phases of calcium carbonate (aragonite, calcite, ikaite and MHC). The grey line represents the linear regression between the values of σ_{calc} and δ_{exp}, based on the equation $\sigma_{calc} = \sigma_{ref} - \delta_{exp}$ (i.e., imposing a gradient = –1), corresponding to σ_{ref} = (170.2 ± 0.7) ppm.

For DFT-GIPAW calculations of solid-state ^{1}H NMR data, the isotropic ^{1}H NMR chemical shift (δ_{calc}) for each ^{1}H environment in the crystal structure was determined from the corresponding DFT-GIPAW calculated value of isotropic ^{1}H NMR shielding (σ_{calc}) using the following equation:

$$\delta_{calc} = \sigma_{ref} - g\,\sigma_{calc} \qquad (3)$$

The values σ_{ref} = 29.61 ppm and g = 0.9643 were taken from a study of α-D-glucose by Brouwer *et al.*[92]

4.6 Procedure for Fitting the ^{13}C Chemical Shift Anisotropy (CSA) Powder Pattern

To compare the experimental ^{13}C CSA powder pattern for CCHH with DFT-GIPAW calculated values of ^{13}C CSA parameters for the monoclinic and orthorhombic structures, the calculated ^{13}C CSA powder patterns were generated using the method of Bloembergen and Rowland,[93] which uses complete elliptic integrals of the first kind. This method uses the algebraic function for the lineshape. More details of the procedure for analysis of the experimental ^{13}C CSA data are given in Section S2.

Acknowledgments

Gaspard Sahuc and Lucas Bind are warmly thanked for their assistance in the CCHH synthesis. This work received funding from the European Research Council (ERC) under the European Union Horizon 2020 Research and Innovation Programme (Grant 758498), and from Agence Nationale de la Recherche (Grant ANR-22-CE29-0002-01). This work was granted access to the HPC resources of Aix-Marseille Université financed by the project Equip@Meso (ANR-10-EQPX-29-01) of the program "Investissements d'Avenir" supervised by the Agence Nationale de la Recherche. We are grateful to Cardiff University for financial support, and to Supercomputing Wales for access to the Hawk HPC facility, which is part-funded by the European Regional Development Fund via the Welsh Government and GW4.

Supporting Information

Solid-State NMR Data for Different Phases of Calcium Carbonate, Additional Analysis of the Experimental 13C CSA Data for CCHH, Additional Powder X-ray Diffraction Data for CCHH, Comparison of the Monoclinic and Orthorhombic Structures, Further DFT-D Geometry Optimization and DFT-GIPAW Calculations on the Monoclinic Structure.

Data Availability

The research data supporting this publication are available at: https://doi.org/10.5281/zenodo.17912836

References

1. Morse, J. W.; Arvidson, R. S.; Lüttge, A., Calcium Carbonate Formation and Dissolution. *Chem. Rev.* **2007,** *107*, 342-381.

2. Millero, F. J., The Marine Inorganic Carbon Cycle. *Chem. Rev.* **2007,** *107*, 308-341.

3. Gower, L. B., Biomimetic Model Systems for Investigating the Amorphous Precursor Pathway and Its Role in Biomineralization. *Chem. Rev.* **2008,** *108*, 4551-4627.

4. Jones, B., Review of calcium carbonate polymorph precipitation in spring systems. *Sediment. Geol.* **2017,** *353*, 64-75.

5. Stolarski, J.; van Dijk, I.; Benning, L. G., Controls on $CaCO_3$ Polymorphism: From Laboratory Precipitation to Biomineralization across Geological Time. *Elements* **2025,** *21*, 92-97.

6. Gebauer, D.; Völkel, A.; Cölfen, H., Stable Prenucleation Calcium Carbonate Clusters. *Science* **2008,** *322*, 1819-1822.

7. Pouget, E. M.; Bomans, P. H. H.; Goos, J. A. C. M.; Frederik, P. M.; With, G. D.; Sommerdijk, N. A. J. M., The Initial Stages of Template-Controlled $CaCO_3$ Formation Revealed by Cryo-TEM. *Science* **2009,** *323*, 1455-1458.

8. Nielsen, M. H.; Aloni, S.; De Yoreo, J. J., In situ TEM imaging of $CaCO_3$ nucleation reveals coexistence of direct and indirect pathways. *Science* **2014,** *345*, 1158-1162.

9. Falini, G.; Albeck, S.; Weiner, S.; Addadi, L., Control of Aragonite or Calcite Polymorphism by Mollusk Shell Macromolecules. *Science* **1996,** *271*, 67-69.

10. Navrotsky, A., Energetic clues to pathways to biomineralization: Precursors, clusters, and nanoparticles. *Proc. Natl. Acad. Sci. U. S. A.* **2004,** *101*, 12096-12101.

11. Xu, A.-W.; Ma, Y.; Cölfen, H., Biomimetic mineralization. *J. Mater. Chem.* **2007,** *17*, 415-449.

12. Nudelman, F.; Sommerdijk, N. A. J. M., Biomineralization as an Inspiration for Materials Chemistry. *Angew. Chem. Int. Ed.* **2012,** *51*, 6582-6596.

13. Anbu, P.; Kang, C.-H.; Shin, Y.-J.; So, J.-S., Formations of calcium carbonate minerals by bacteria and its multiple applications. *SpringerPlus* **2016,** *5*, 250.

14. Bragg, W. L., The analysis of crystals by the X-ray spectrometer. *Proc. Roy. Soc. A* **1914,** *89*, 468-489.

15. Wyckoff, R. W. G., The Crystal Structures of Some Carbonates of the Calcite Group. *Am. J. Sci.* **1920,** *50*, 317-360.

16. Bragg, W. H., IX. Bakerian Lecture.— X-rays and crystal structure. *Phil. Trans. Roy. Soc. A* **1915,** *215*, 253-274.

17. Maslen, E. N.; Streltsov, V. A.; Streltsova, N. R., X-ray study of the electron density in calcite, $CaCo_3$. *Acta Crystallogr. B* **1993,** *49*, 636-641.

18. Bevan, D. J. M.; Rossmaith, E.; Mylrea, D. K.; Ness, S. E.; Taylor, R. M.; Cuff, C., On the structure of aragonite - Lawrence Bragg revisited. *Acta Crystallogr. Sect. B* **2002,** *58*, 448-456.

19. Pokroy, B.; Quintana, J. P.; Caspi, E. A. N.; Berner, A.; Zolotoyabko, E., Anisotropic lattice distortions in biogenic aragonite. *Nat. Mater.* **2004,** *3*, 900-902.

20. Bragg, W. L., The structure of aragonite. *Proc. Roy. Soc. A* **1924,** *105*, 16-39.

21. Olshausen, S. v., XXVII. Strukturuntersuchungen nach der Debye-Scherrer-Methode. *Z. Kristallogr.* **1924,** *61*, 463-514.

22. Kamhi, S., On the structure of vaterite $CaCO_3$. *Acta Crystallogr.* **1963,** *16*, 770-772.

23. Mugnaioli, E.; Andrusenko, I.; Schüler, T.; Loges, N.; Dinnebier, R. E.; Panthöfer, M.; Tremel, W.; Kolb, U., Ab Initio Structure Determination of Vaterite by Automated Electron Diffraction. *Angew. Chem. Int. Ed.* **2012,** *51*, 7041-7045.

24. Kabalah-Amitai, L.; Mayzel, B.; Kauffmann, Y.; Fitch, A. N.; Bloch, L.; Gilbert, P. U. P. A.; Pokroy, B., Vaterite Crystals Contain Two Interspersed Crystal Structures. *Science* **2013,** *340*, 454-457.

25. Burgess, K. M. N.; Bryce, D. L., On the crystal structure of the vaterite polymorph of CaCO3: A calcium-43 solid-state NMR and computational assessment. *Solid State Nucl. Magn. Reson.* **2015,** *65*, 75-83.

26. Christy, A. G., A Review of the Structures of Vaterite: The Impossible, the Possible, and the Likely. *Cryst. Growth Des.* **2017,** *17*, 3567-3578.

27. Jamieson, J. C., Phase Equilibrium in the System Calcite-Aragonite. *J. Chem. Phys.* **1953,** *21*, 1385-1390.

28. Meldrum, F. C., Calcium carbonate in biomineralisation and biomimetic chemistry. *Int. Mater. Rev.* **2003,** *48*, 187-224.

29. Sekkal, W.; Zaoui, A., Nanoscale analysis of the morphology and surface stability of calcium carbonate polymorphs. *Sci. Rep.* **2013,** *3*, 1587.

30. Lennie, A. R.; Tang, C. C.; Thompson, S. P., The structure and thermal expansion behaviour of ikaite, CaCO3.6H2O, from T=114 to T=293 K. *Mineral. Mag.* **2004,** *68*, 135-146.

31. Dickens, B.; Brown, W. E., Crystal structure of calcium carbonate hexahydrate at about -120.deg. *Inorg. Chem.* **1970,** *9*, 480-486.

32. Hesse, K. F.; Kueppers, H.; Suess, E. Z., Refinement of the structure of Ikaite, CaCO3 · 6H2O. *Z. Kristallogr.* **1983,** *163*, 227-231.

33. Effenberger, H., Kristallstruktur und Infrarot-Absorptionsspektrum von synthetischem Monohydrocalcit, CaCO3·H2O. *Monatshefte für Chemie / Chemical Monthly* **1981,** *112*, 899-909.

34. Swainson, I. P., The structure of monohydrocalcite and the phase composition of the beachrock deposits of Lake Butler and Lake Fellmongery, South Australia. *Amer. Mineral.* **2008,** *93*, 1014-1018.

35. Zou, Z.; Habraken, W. J. E. M.; Matveeva, G.; Jensen, A. C. S.; Bertinetti, L.; Hood, M. A.; Sun, C.-y.; Gilbert, P. U. P. A.; Polishchuk, I.; Pokroy, B.; Mahamid, J.; Politi, Y.; Weiner, S.; Werner, P.; Bette, S.; Dinnebier, R.; Kolb, U.; Zolotoyabko, E.; Fratzl, P., A hydrated crystalline calcium carbonate phase: Calcium carbonate hemihydrate. *Science* **2019,** *363*, 396-400.

36. Marland, G., The stability of CaCO3·6H2O (ikaite). *Geochim. Cosmochim. Acta* **1975,** *39*, 83-91.

37. Tateno, N.; Kyono, A., Structural change induced by dehydration in ikaite ($CaCO_3 \cdot 6H_2O$). *J. Mineral. Petrolog. Sci.* **2014,** *109*, 157-168.

38. Kimura, T.; Koga, N., Thermal Dehydration of Monohydrocalcite: Overall Kinetics and Physico-geometrical Mechanisms. *J. Phys. Chem. A* **2011,** *115*, 10491-10501.

39. Addadi, L.; Raz, S.; Weiner, S., Taking advantage of disorder: Amorphous calcium carbonate and its roles in biomineralization. *Adv. Mater.* **2003,** *15*, 959-970.

40. Michel, F. M.; MacDonald, J.; Feng, J.; Phillips, B. L.; Ehm, L.; Tarabrella, C.; Parise, J. B.; Reeder, R. J., Structural Characteristics of Synthetic Amorphous Calcium Carbonate. *Chem. Mater.* **2008,** *20*, 4720-4728.

41. Stephens, C. J.; Ladden, S. F.; Meldrum, F. C.; Christenson, H. K., Amorphous Calcium Carbonate is Stabilized in Confinement. *Adv. Funct. Mater.* **2010,** *20*, 2108-2115.

42. Radha, A. V.; Forbes, T. Z.; Killian, C. E.; Gilbert, P. U. P. A.; Navrotsky, A., Transformation and crystallization energetics of synthetic and biogenic amorphous calcium carbonate. *Proc. Natl. Acad. Sci. U. S. A.* **2010,** *107*, 16438-16443.

43. Goodwin, A. L.; Michel, F. M.; Phillips, B. L.; Keen, D. A.; Dove, M. T.; Reeder, R. J., Nanoporous Structure and Medium-Range Order in Synthetic Amorphous Calcium Carbonate. *Chem. Mater.* **2010,** *22*, 3197-3205.

44. Gebauer, D.; Gunawidjaja, P. N.; Ko, J. Y. P.; Bacsik, Z.; Aziz, B.; Liu, L.; Hu, Y.; Bergström, L.; Tai, C.-W.; Sham, T.-K.; Edén, M.; Hedin, N., Proto-Calcite and Proto-Vaterite in Amorphous Calcium Carbonates. *Angew. Chem. Int. Ed.* **2010,** *49*, 8889-8891.

45. Cartwright, J. H. E.; Checa, A. G.; Gale, J. D.; Gebauer, D.; Sainz-Diaz, C. I., Calcium Carbonate Polyamorphism and Its Role in Biomineralization: How Many Amorphous Calcium Carbonates Are There? *Angew. Chem. Int. Ed.* **2012,** *51*, 11960-11970.

46. Nicholas, T. C.; Stones, A. E.; Patel, A.; Michel, F. M.; Reeder, R. J.; Aarts, D. G. A. L.; Deringer, V. L.; Goodwin, A. L., Geometrically frustrated interactions drive structural complexity in amorphous calcium carbonate. *Nat. Chem.* **2024,** *16*.

47. Nebel, H.; Neumann, M.; Mayer, C.; Epple, M., On the Structure of Amorphous Calcium Carbonate—A Detailed Study by Solid-State NMR Spectroscopy. *Inorg. Chem.* **2008,** *47*, 7874-7879.

48. Wang, Y. W.; Kim, Y. Y.; Stephens, C. J.; Meldrum, F. C.; Christenson, H. K., In Situ Study of the Precipitation and Crystallization of Amorphous Calcium Carbonate (ACC). *Cryst. Growth Des.* **2012,** *12*, 1212-1217.

49. Rodriguez-Blanco, J. D.; Shaw, S.; Benning, L. G., The kinetics and mechanisms of amorphous calcium carbonate (ACC) crystallization to calcite, viavaterite. *Nanoscale* **2011,** *3*, 265-271.

50. Noel, E. H.; Kim, Y.-Y.; Charnock, J. M.; Meldrum, F. C., Solid state crystallization of amorphous calcium carbonate nanoparticles leads to polymorph selectivity. *CrystEngComm* **2013,** *15*, 697-705.

51. Von Euw, S.; Azaïs, T.; Manichev, V.; Laurent, G.; Pehau-Arnaudet, G.; Rivers, M.; Murali, N.; Kelly, D. J.; Falkowski, P. G., Solid-State Phase Transformation and Self-Assembly of Amorphous Nanoparticles into Higher-Order Mineral Structures. *J. Am. Chem. Soc.* **2020,** *142*, 12811-12825.

52. Schmidt, C. A.; Tambutté, E.; Venn, A. A.; Zou, Z.; Castillo Alvarez, C.; Devriendt, L. S.; Bechtel, H. A.; Stifler, C. A.; Anglemyer, S.; Breit, C. P.; Foust, C. L.; Hopanchuk, A.; Klaus, C. N.; Kohler, I. J.; LeCloux, I. M.; Mezera, J.; Patton, M. R.; Purisch, A.; Quach, V.; Sengkhammee, J. S.; Sristy, T.; Vattem, S.; Walch, E. J.; Albéric, M.; Politi, Y.; Fratzl, P.; Tambutté, S.; Gilbert, P. U. P. A., Myriad Mapping of nanoscale minerals reveals calcium carbonate hemihydrate in forming nacre and coral biominerals. *Nat. Commun.* **2024,** *15*, 1812.

53. Aufort, J.; Demichelis, R., Magnesium Impurities Decide the Structure of Calcium Carbonate Hemihydrate. *Cryst. Growth Des.* **2020,** *20*, 8028-8038.

54. Harris, R. K.; Hodgkinson, P.; Pickard, C. J.; Yates, J. R.; Zorin, V., Chemical shift computations on a crystallographic basis: some reflections and comments. *Magn. Reson. Chem.* **2007,** *45*, S174-S186.

55. Bryce, D. L.; Bultz, E. B.; Aebi, D., Calcium-43 chemical shift tensors as probes of calcium binding environments.: Insight into the structure of the vaterite CaCO3 polymorph by 43Ca solid-state NMR spectroscopy. *J. Am. Chem. Soc.* **2008,** *130*, 9282-9292.

56. Harris, R. K.; Hodgkinson, P.; Pickard, C. J.; Yates, J. R.; Zorin, V., Chemical Shift Computations for Crystalline Molecular Systems: Practice. In *eMagRes*, John Wiley & Sons ed.; 2009.

57. Baias, M.; Widdifield, C. M.; Dumez, J.-N.; Thompson, H. P. G.; Cooper, T. G.; Salager, E.; Bassil, S.; Stein, R. S.; Lesage, A.; Day, G. M.; Emsley, L., Powder crystallography of pharmaceutical materials by combined crystal structure prediction and solid-state 1H NMR spectroscopy. *Phys. Chem. Chem. Phys.* **2013,** *15*, 8069-8080.

58. Dudek, M. K.; Kazmierski, S.; Kostrzewa, M.; Potrzebowski, M. J., Solid-State NMR Studies of Molecular Crystals. In *Annual Reports on NMR Spectroscopy, Vol 95*, Webb, G. A., Ed. 2018; Vol. 95, pp 1-81.

59. Paruzzo, F. M.; Hofstetter, A.; Musil, F.; De, S.; Ceriotti, M.; Emsley, L., Chemical shifts in molecular solids by machine learning. *Nat. Commun.* **2018,** *9*, 4501.

60. Hodgkinson, P., NMR crystallography of molecular organics. *Prog. Nucl. Magn. Reson. Spectrosc.* **2020,** *118-119*, 10-53.

61. Southern, S. A.; Bryce, D. L., Chapter One - Recent advances in NMR crystallography and polymorphism. In *Annu. Rep. NMR Spectrosc.*, Webb, G. A., Ed. Academic Press: 2021; Vol. 102, pp 1-80.

62. Smalley, C. J. H.; Hoskyns, H. E.; Hughes, C. E.; Johnstone, D. N.; Willhammar, T.; Young, M. T.; Pickard, C. J.; Logsdail, A. J.; Midgley, P. A.; Harris, K. D. M., A structure determination protocol based on combined analysis of 3D-ED data, powder XRD data, solid-state NMR data and DFT-D calculations reveals the structure of a new polymorph of L-tyrosine. *Chem. Sci.* **2022,** *13*, 5277-5288.

63. Cordova, M.; Moutzouri, P.; Nilsson Lill, S. O.; Cousen, A.; Kearns, M.; Norberg, S. T.; Svensk Ankarberg, A.; McCabe, J.; Pinon, A. C.; Schantz, S.; Emsley, L., Atomic-level structure determination of amorphous molecular solids by NMR. *Nat. Commun.* **2023,** *14*, 5138.

64. Cousin, S. F.; Hughes, C. E.; Ziarelli, F.; Viel, S.; Mollica, G.; Harris, K. D. M.; Pinon, A. C.; Thureau, P., Exploiting solid-state dynamic nuclear polarization NMR spectroscopy to establish the spatial distribution of polymorphic phases in a solid material. *Chem. Sci.* **2023,** *14*, 10121-10128.

65. Rahman, M.; Dannatt, H. R. W.; Blundell, C. D.; Hughes, L. P.; Blade, H.; Carson, J.; Tatman, B. P.; Johnston, S. T.; Brown, S. P., Polymorph Identification for Flexible Molecules: Linear Regression Analysis of Experimental and Calculated Solution- and Solid-State NMR Data. *J. Phys. Chem. A* **2024,** *128*, 1793-1816.

66. Smalley, C. J. H.; Hughes, C. E.; Hildebrand, M.; Aizen, R.; Bauer, M.; Yamano, A.; Levy, D.; Mirsky, S. K.; Shaked, N. T.; Young, M. T.; Kolb, U.; Gazit, E.; Kronik, L.; Harris, K. D. M., Understanding the Solid-State Structure of Riboflavin through a Multitechnique Approach. *Cryst. Growth Des.* **2024,** *24*, 6256-6266.

67. Emsley, L., Spiers Memorial Lecture: NMR crystallography. *Faraday Discuss.* **2025,** *255*, 9-45.

68. Ramos, S. A.; Mueller, L. J.; Beran, G. J. O., The interplay of density functional selection and crystal structure for accurate NMR chemical shift predictions. *Faraday Discuss.* **2025,** *255*, 119-142.

69. Juramy, M.; Besson, E.; Gastaldi, S.; Ziarelli, F.; Viel, S.; Mollica, G.; Thureau, P., Exploring the crystallisation of aspirin in a confined porous material using solid-state nuclear magnetic resonance. *Faraday Discuss.* **2025,** *255*, 483-494.

70. Clark, S. J.; Segall, M. D.; Pickard, C. J.; Hasnip, P. J.; Probert, M. I. J.; Refson, K.; Payne, M. C., First principles methods using CASTEP. *Z. Kristallogr.* **2005,** *220*, 567-570.

71. Pickard, C. J.; Mauri, F., All-electron magnetic response with pseudopotentials: NMR chemical shifts. *Phys. Rev. B* **2001,** *63*, 245101.

72. Yates, J. R.; Pickard, C. J.; Mauri, F., Calculation of NMR chemical shifts for extended systems using ultrasoft pseudopotentials. *Phys. Rev. B* **2007,** *76*, 024401.

73. Bonhomme, C.; Gervais, C.; Babonneau, F.; Coelho, C.; Pourpoint, F.; Azaïs, T.; Ashbrook, S. E.; Griffin, J. M.; Yates, J. R.; Mauri, F.; Pickard, C. J., First-Principles Calculation of NMR Parameters Using the Gauge Including Projector Augmented Wave Method: A Chemist's Point of View. *Chem. Rev.* **2012,** *112*, 5733-5779.

74. Dudenko, D. V.; Williams, P. A.; Hughes, C. E.; Antzutkin, O. N.; Velaga, S. P.; Brown, S. P.; Harris, K. D. M., Exploiting the Synergy of Powder X-ray Diffraction and Solid-State NMR Spectroscopy in Structure Determination of Organic Molecular Solids. *J. Phys. Chem. C* **2013,** *117*, 12258-12265.

75. Xu, M.; Harris, K. D. M., Altering the Polymorphic Product Distribution in a Solid-State Dehydration Process by Rapid Sample Rotation in a Solid-State NMR Probe. *J. Am. Chem. Soc.* **2005,** *127*, 10832-10833.

76. Hughes, C. E.; Williams, P. A.; Keast, V. L.; Charalampopoulos, V. G.; Edwards-Gau, G. R.; Harris, K. D. M., New in situ solid-state NMR techniques for probing the evolution of crystallization processes: pre-nucleation, nucleation and growth. *Faraday Discuss.* **2015,** *179*, 115-140.

77. Hughes, C. E.; Ratnasingam, N. V.; Williams, P. A.; Benhenou, E.; Patterson, R.; Harris, K. D. M., NMR crystallization: in situ NMR strategies for monitoring the evolution of crystallization processes. *Faraday Discuss.* **2025,** *255*, 520-552.

78. Liu, S. F.; Mao, J. D.; Schmidt-Rohr, K., A Robust Technique for Two-Dimensional Separation of Undistorted Chemical-Shift Anisotropy Powder Patterns in Magic-Angle-Spinning NMR. *J. Magn. Reson.* **2002,** *155*, 15-28.

79. Taylor, R. E., ^{13}C CP/MAS: Application to Glycine. *Concepts Magn. Reson.* **2004,** *22A*, 79-89.

80. Cerreia Vioglio, P.; Mollica, G.; Juramy, M.; Hughes, C. E.; Williams, P. A.; Ziarelli, F.; Viel, S.; Thureau, P.; Harris, K. D. M., Insights into the Crystallization and Structural Evolution of Glycine Dihydrate by In Situ Solid-State NMR Spectroscopy. *Angew. Chem. Int. Ed.* **2018,** *57*, 6619-6623.

81. Fung, B. M.; Khitrin, A. K.; Ermolaev, K., An Improved Broadband Decoupling Sequence for Liquid Crystals and Solids. *J. Magn. Reson.* **2000,** *142*, 97-101.

82. Marion, D.; Ikura, M.; Tschudin, R.; Bax, A., Rapid recording of 2D NMR spectra without phase cycling. Application to the study of hydrogen exchange in proteins. *J. Magn. Reson.* **1989,** *85*, 393-399.

83. Van Geet, A. L., Calibration of the methanol and glycol nuclear magnetic resonance thermometers with a static thermistor probe. *Anal. Chem.* **1968,** *40*, 2227-2229.

84. Yamamoto, O.; Yanagisawa, M., Method for calibration of nuclear magnetic resonance standard samples for measuring temperature. *Anal. Chem.* **1970,** *42*, 1463-1465.

85. Findeisen, M.; Brand, T.; Berger, S., A 1H-NMR thermometer suitable for cryoprobes. *Magn. Reson. Chem.* **2007,** *45*, 175-178.

86. Vanderbilt, D., Soft self-consistent pseudopotentials in a generalized eigenvalue formalism. *Phys. Rev. B* **1990,** *41*, 7892-7895.

87. Perdew, J. P.; Burke, K.; Ernzerhof, M., Generalized Gradient Approximation Made Simple. *Phys. Rev. Lett.* **1996,** *77*, 3865-3868.

88. Tkatchenko, A.; Scheffler, M., Accurate Molecular Van Der Waals Interactions from Ground-State Electron Density and Free-Atom Reference Data. *Phys. Rev. Lett.* **2009,** *102*, 073005.

89. Monkhorst, H. J.; Pack, J. D., Special points for Brillouin-zone integrations. *Phys. Rev. B* **1976,** *13*, 5188-5192.

90. Jarosch, D.; Heger, G., Neutron diffraction refinement of the crystal structure of aragonite. *Tschermaks Mineral. Petrogr. Mitt.* **1986,** *35*, 127-131.

91. Sitepu, H., Texture and structural refinement using neutron diffraction data from molybdite (MoO3) and calcite (CaCO3) powders and a Ni-rich Ni50.7Ti49.30 alloy. *Powder Diffr.* **2009,** *24*, 315-326.

92. Brouwer, D. H.; Mikolajewski, J. G., A combined solid-state NMR and quantum chemical calculation study of hydrogen bonding in two forms of α-d-glucose. *Solid State Nucl. Magn. Reson.* **2023,** *123*, 101848.

93. Bloembergen, N.; Rowland, T. J., On the nuclear magnetic resonance in metals and alloys. *Acta Metallurgica* **1953,** *1*, 731-746.

For Table of Contents Use Only

Table of Contents Graphic

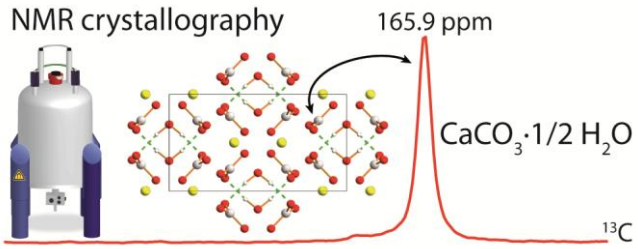

The structure of calcium carbonate hemihydrate is explored using NMR crystallography

Title: New Insights into the Structural Properties of Calcium Carbonate Hemihydrate by NMR Crystallography

Authors: Romain Chèvre,[1] Colan E. Hughes,[2] Samuel F. Cousin,[1] Marie Juramy,[1] Fabio Ziarelli,[3] Stéphane Viel,[1,4] Kenneth D. M. Harris,*[,2] Giulia Mollica,*[,1] Pierre Thureau*[,1]